Geomechanics and Engineering, *Vol. 33, No. 6 (2023) 597-609*
https://doi.org/10.12989/gae.2023.33.6.597

Crack initiation mechanism and meso-crack evolution of pre-fabricated cracked sandstone specimens under uniaxial loading

Bing Sun*[1], Haowei Yang[1a], Sheng Zeng**[2], Yu Yin[2,3b] and Junwei Fan[1c]

[1]*School of Civil Engineering, University of South China, Hengyang, Hunan 421001, PR China*
[2]*School of Resources Environment and Safety Engineering, University of South China, Hengyang, Hunan 421001, PR China*
[3]*Sinosteel Maanshan General Institute of Mining Research Co., Ltd., Maanshan, Anhui 243000, PR China*

(*Received November 2, 2022, Revised April 25, 2023, Accepted May 4, 2023*)

Abstract. The instability and failure of engineered rock masses are influenced by crack initiation and propagation. Uniaxial compression and acoustic emission (AE) experiments were conducted on cracked sandstone. The effect of the crack's dip on the crack initiation was investigated using fracture mechanics. The crack propagation was investigated based on stress-strain curves, AE multi-parameter characteristics, and failure modes. The results show that the crack initiation occurs at the tip of the pre-fabricated crack, and the crack initiation angle increases from 0° to 70° as the dip angle increases from 0° to 90°. The fracture strength k_{cr} is derived varies in a U-shaped pattern as β increased, and the superior crack angle β_m is between 36.2 and 36.6 and is influenced by the properties of the rock and the crack surface. Low-strength, large-scale tensile cracks form during the crack initiation in the cracked sandstone, corresponding to the start of the AE energy, the first decrease in the *b*-value, and a low *r*-value. When macroscopic surface cracks form in the cracked sandstone, high-strength, large-scale shear cracks form, resulting in a rapid increase in the AE energy, a second decrease in the *b*-value and an abrupt increase in the *r*-value. This research has significant theoretical implications for rock failure mechanisms and establishment of damage indicators in underground engineering.

Keywords: acoustic emission; fracture mechanics; meso-crack evolution; pre-fabricated cracked sandstone; uniaxial compression

1. Introduction

Natural rock evolves through time into a material with inherent defects, containing an abundance of discontinuous structural planes such as cracks, holes, and joints. These discontinuous structural plane defects significantly reduce the rock mass' strength. Moreover, when external loads are applied, these defects easily cause crack initiation, expansion, and penetration, as well as determine the characteristics of crack propagation (Wu *et al*. 2021, Sun *et al*. 2023). According to engineering practice, the formation of new cracks in a rock and the initiation of the original cracks signal the start of the rupturing of the rock mass. Numerous instabilities and failures of geotechnical engineering are induced by the initiation-expansion-penetration of interior cracks in a rock mass (Wu *et al*. 2021, Sun *et al*. 2021, Yuan *et al*. 2020). As a result, it is advantageous to investigate the crack initiation and propagation characteristics of prefabricated cracked rock specimens in order to reveal the failure mechanism and instability features of engineered rock masses.

Currently, research on the mechanisms of crack initiation and propagation in rock is mainly divided into three categories: theoretical studies, numerical simulations, and experimental studies. The basic idea is to propose a model or method first and then validate it through experiments or numerical simulations. In terms of theoretical studies, there are several criteria for crack initiation, including the maximum circumferential stress (Erdogan and Sih 1963), maximum shear stress (Lin 1985), minimum strain energy density (Sih 1974), and maximum distortion energy (Guo *et al*. 2019). Liu (2019) introduced *T*-stress into the classical MTS criterion, and proposed a new MTS criterion considering t stress. Tang (2015) investigated the effect of *T*-stress on the initiation and propagation of cracks in a compression-shear state rock. Numerous investigations (Zhao *et al*. 2018, Lu and Meshii 2014) have shown that for rocks in a compression-shear state, when the singular stress term and the constant term at the crack tip are included in the stress field at the crack tip, the results of the calculation are significantly improved. The constant stress term parallel to the crack surface is called *T*-stress in fracture mechanics (Shlyannikov 2013). The angle and fracture strength were computed more accurately using the *T*-stress fracture criteria than using conventional

∗Corresponding author, Ph.D.
E-mail: sunbingnh@126.com
**Corresponding author, Ph.D.
E-mail: usczengs@126.com
[a]M.D. Student
E-mail: yangssi1987@126.com
[b]Senior Engineer
E-mail: 458420349@qq.com
[c]Lecturer
E-mail: 407713159@qq.com

ISSN: 2005-307X (Print), 2092-6219 (Online)

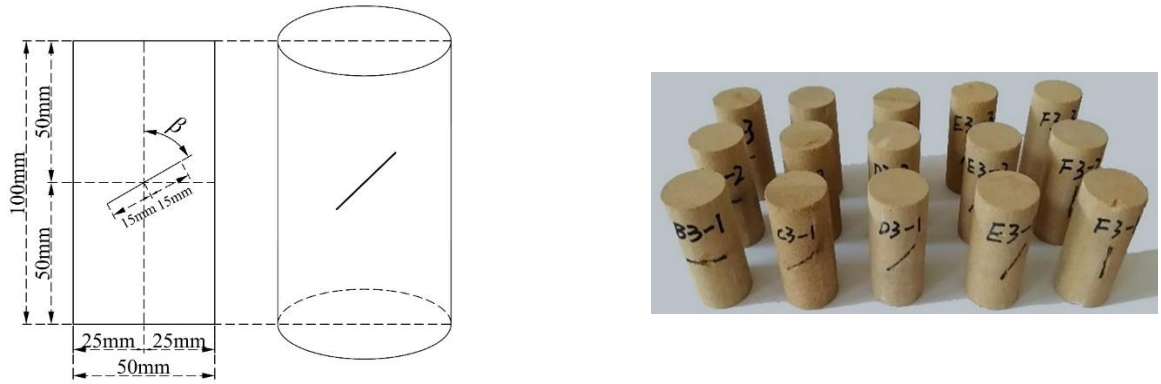

(a) (b)

Fig. 1 Image of cracked sandstone sample

theories (Li *et al*. 2020, Aliha *et al*. 2017). With the development of computers, research on numerical simulations in crack propagation has increased. Haeri H *et al*. (2020) employed the extended finite element method to verify that tensile cracking is the main mechanism of crack initiation at the crack tip in mortar. Abdollahipour *et al*. (2016, 2020) used the displacement discontinuity method (DDM) to investigate crack propagation in porous elastic media, as well as the influence of thermal coupling on crack propagation. Rezanezhad *et al*. (2020, 2021) utilized the extended finite element method (XFEM) to demonstrate that the shape of pores have significant impacts on the crack propagation path. The evolution of cracks within rock is extremely complex, which is largely attributed to the inhomogeneity, dispersion, and anisotropy of factors. It is difficult to clearly identify the laws governing crack evolution (Li *et al.* 2021, Sun *et al.* 2023). AE technology, which enables real-time monitoring of microcracks, has become a valuable research tool in this area. AE is the phenomenon in which a rock deforms or ruptures as a result of stress deformation and failure and releases strain energy in the form of elastic waves (Zhang *et al*. 2021, Zhang *et al*. 2019). Based on AE tests, Ganne *et al*. (2007) identified four stages of AE energy accumulation, which correspond to the formation, expansion, accumulation, and aggregation of micro-cracks, as well as the occurrence of ultimate rock failure. Kim *et al*. (2015) performed macroscopic deformation and AE tests on granite simultaneously and discovered that the AE energy is more sensitive than macroscopic deformation for monitoring crack initiation and propagation. Liu *et al* (2019) conducted brazilian splitting tests and uniaxial compression tests on limestone and discovered that the development of the *b*-value occur in distinct stages under the two loading regimes. Wang *et al*. (2012) analyzed the four stages of the evolution of micro-cracks in dissolution pore limestone using the *RA*-*AF* value. It was found that using AE characteristic parameters to determine the evolution characteristics of rock meso-cracks is a sound technological approach.

The results of previous studies have contributed to the improvement of our understanding of the characteristics of rock crack initiation and propagation. However, due to the extremely complicated nature of the crack initiation mechanism in cracked rocks, it is important to conduct more theoretical research on the effect of the crack dip on the crack initiation characteristics. Moreover, several factors contribute to the variations in the AE characteristic parameters, which can be used to describe the rock's meso-crack activities, and the rock failure process is complicated. Using a small number of parameters to study the rupture features of a rock may easily lead to the omission of critical information. Thus, in this study, uniaxial compression and AE experiments were conducted on intact sandstone and sandstone containing a prefabricated crack with dips of 0°, 30°, 45°, 60°, and 90°. The crack initiation mechanism of the cracked sandstone was investigated using fracture mechanics. The superior crack angle was defined and properties affected by the rock and the crack surface were obtained. Based on fracture mechanics, the functional relationship between rock fracture strength and crack dip angle was derived. The laws of the angle of crack tip initiation and rock fracture strength as a change of the crack dip angle are obtained. The strength and deformation features of the cracked sandstone are investigated based on the stress-strain data, macroscopic failure mode, and AE parameters. The evolution laws of the meso-crack initiation, propagation, and penetration are analyzed, and the differences and relevance in the evolution of the AE parameters during the various stages of crack propagation are clarified

2. Experiment

2.1 Sample preparation

The sample was collected from a Hunan construction site and is representative of the most common yellow sandstone in southern China. Standard cylindrical rock specimens (50 mm × 100 mm) were prepared in accordance with the International Society for Rock Mechanics (ISRM) standards. To create a crack that cut through the specimen and met the test requirements, a small hole with a diameter of 1–2 mm was drilled in the center of the specimens along its axis. A 0.30 mm emery steel wire was passed through this small hole. The length of the sawing was 30 mm, and

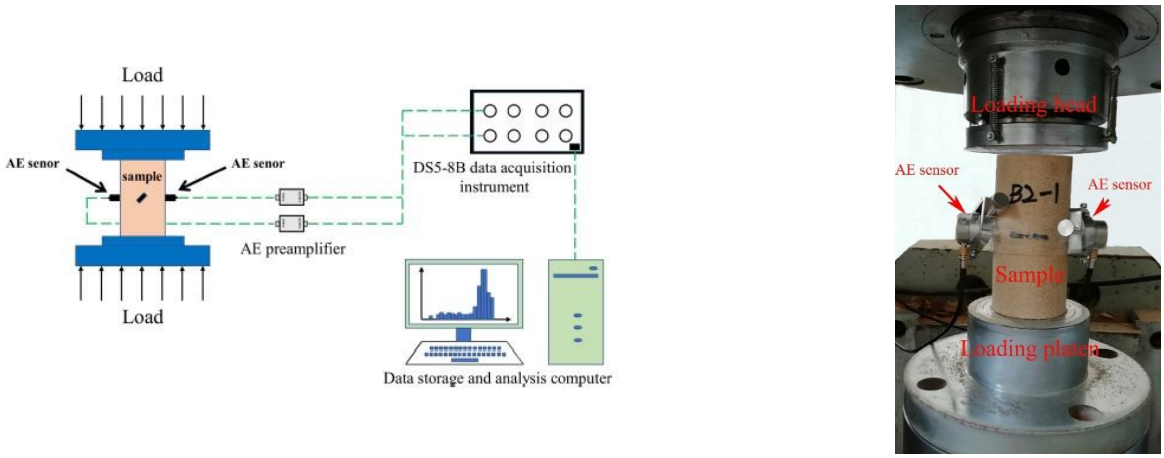

(a) Acoustic emission system (b) Acoustic emission device

Fig. 2 Schematic diagram of the acoustic emission acquisition system used for the sandstone loading and failure experiments

the average thickness of the prefabricated cracks was 0.5–0.7 mm. Following the method (Wang *et al*. 2019), cracks with dip angles of 0°, 30°, 45°, 60°, and 90° were cut in the specimens. After the samples were prepared, they were sorted and numbered; each group contained three specimens, and the particular groups were labeled as follows: A, B3, C3, D3, E3, and F3 (numbering conventions are as follows: letters A, B, C, D, E, and F denote no crack and cracks with dip angles of 90°, 60°, 45°, 30°, and 0°, respectively). The number 3 after the letter indicates that the fracture is 30 mm length. The sample preparation procedure is shown in Fig. 1.

2.2 Experiment methods

The loading control system used was an RMT150-B test machine produced by the Institute of Rock and Soil Mechanics, Chinese Academy of Sciences. The loading method was force-controlled with a loading rate of 1 kN/s, according to the ISRM specifications. The AE data were acquired using a DS5-8B multi-channel synchronous acquisition system (Beijing Soft Island Times Technology Co., Ltd., China, Beijing). To ensure that the cylindrical sample's surface fit snugly against the AE sensor's surface, one end of the sample was attached to the sensor and the other end was attached to a tiny transition device on the sensor's surface. Each sensor contained a pre-amplifier. The threshold of all of the sensors was set to 45 dB, and the pre-amplifier gain was set to 40 dB. Fig. 2 shows the testing system.

The tests were performed in the force-controlled loading mode. Prior to each test, the top and lower ends of the sample were coated with butter to minimize the friction and noise between the loading plane and the sample during compression. To minimize the loss of AE signals, two AE sensors were positioned on the sample's surface, vaseline was applied between the AE sensor and the sample, and then, the sensor was secured using adhesive tape to guarantee excellent contact. Prior to the test, the sensor's response was measured to determine the amplitude of the analog signal source's response, and the test was started once the sensor's response was verified to be normal. During the test, a 500 N pre-loading force was applied to the sample to ensure that the platen made complete contact with the sample. The pressure and the data collection instrument's data storage function were simultaneously initiated according to the preset test plan. The AE signals were recorded and stored during the loading operation.

3. Experimental results and analysis

3.1 Stress-strain curve

According to the average values of elastic modulus and strength that obtained from a group of rock samples, the stress-strain curve closest to the average value was selected as the test result. The stress-strain curves for the intact sample and the cracked samples are shown in Fig. 3. The stress-strain curves of the sandstone samples with different crack dip angles exhibit stages of compaction, linear elastic deformation, yield, and failure. Due to the presence of initial micro-defects in the natural sandstone, the first loading stage result in the nonlinear development of axial stress and strain. The 30° sample has long compaction stage. After undergoing linear elastic deformation, the stress-strain curve of the 60° sample is always below the stress-strain curve of the other rock samples, and the difference increase with increasing stress. Thus, the elastic modulus of the 60° sample is lower than the elastic modulus of the other rock samples. Due to the presence of a pre-fabricated crack, the mechanical characteristics of the cracked samples exhibit variable degrees of degradation, with a lower strength than the intact sample.

3.2 Strength characteristics

The initiation stress indicates the initiation of the accumulation of the damage to the rock. One technique of determining the initiation stress is to monitor the stress

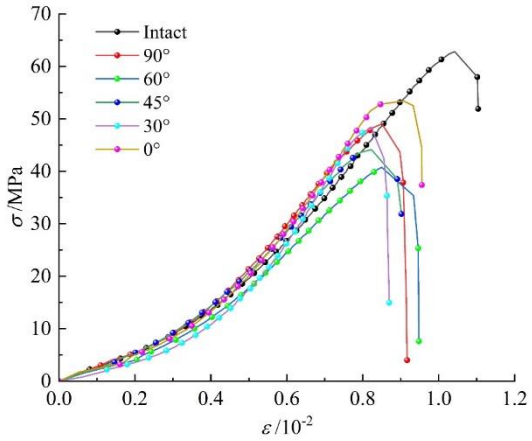

Fig. 3 Stress-strain curves of the cracked samples with different dip angles

value associated with the initiation time of the crack propagation on the rock's surface. The other is to use an AE test to monitor all of the fracture activity inside the rock. Indeed, the crack propagation in the rock is three-dimensional, and prior to the formation of macroscopic surface cracks, the interior micro-cracks are already active. AE monitoring signals are more sensitive to micro-fracturing and thus can more precisely depict the first formation of interior cracks. Zhang *et al*. (2021) discovered that the crack initiation stress measured using a camera was much larger than that measured using the AE signal in an AE test conducted on granite. Additionally, our research revealed that the initiation and propagation of surface cracks occurred in certain samples extremely quickly prior to failure. Thus, in order to precisely determine the crack initiation stress of the cracked sandstone, in this study, the crack initiation stress was defined as the stress when the AE energy counting rate become substantial (Eberhard *et al*. 1998).

The strength characteristics of the cracked sandstone samples were analyzed. As can be seen from Fig. 4, the peak strength σ_c, crack initiation stress σ_{ci}, and crack initiation stress level $R_{ci}(\sigma_{ci}/\sigma_c)$ all fluctuate with the crack dip angle. The dip angle of the crack has a significant effect on the crack initiation stress and peak strength. The crack initiation stress decrease from 9.38 MPa to 6.52 MPa and subsequently increase to 9.21 MPa as the crack dip angle increased, and the crack initiation stress is around 13–20% of the peak stress, suggesting that the crack initiation occur relatively early inside the rock. The peak strength initially decreases from 53.42 MPa to 40.69 MPa and then increase to 49.03 MPa, producing concave curves that initially decrease and then increase. Thus, the dip angle of the crack has a considerable influence on the crack initiation and rock failure.

3.3 Failure modes

Fig. 5 shows the failure modes of the sandstone samples with different crack angles when subjected to uniaxial compression. The cracks are mostly tensile (T) and shear

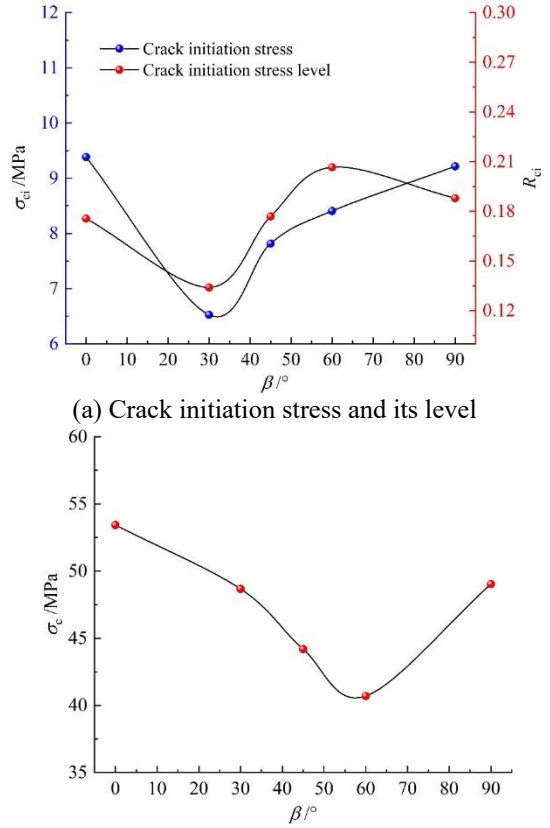

(a) Crack initiation stress and its level

(b) Peak strength

Fig. 4 Samples' strength characteristics as a relationship of crack dip angle

(S) cracks. The shear stress generates shear cracks at the top and bottom of the intact sample, which subsequently connect with the tensile cracks to form multiple longitudinal macro-cracks that run the length of the sample. A tensile crack with a small angle initiates in the left side of the 0° sample's crack tip first, and then, the shear cracks at the sample's top and bottom pass through the pre-fabricated cracked plane, which is a typical shear failure mode. Due to the action of the tensile stress, the pre-fabricated crack tips of the 30° and 45° samples generate wing cracks first. By observing the displacement before and after the pre-fabricated cracks propagate, it is determined that the pre-fabricated cracks behaved as sliding-type cracks, but they subsequently develop as shear cracks due to the action of the shear stress. The number of tensile cracks rapidly increase as the dip angle β of the crack increased. When $\beta \leq 45°$, the sample is easily affected by the shear stress, resulting in an increase in the number of shear cracks in the sample during the crack propagation stage. When $\beta \geq 60°$, the tensile cracks are predominant, and the crack tip forms a wing crack first, with a large angle between the wing crack and the pre-fabricated crack, under the action of tensile stress. It extends along the load direction to the bottom of the sample. Few shear cracks also form.

Although the cracked samples fail as a result of the cracking of the original defects under concentrated tensile stress, the different parameters of the defects necessarily result in a fundamental variation in the modes of crack

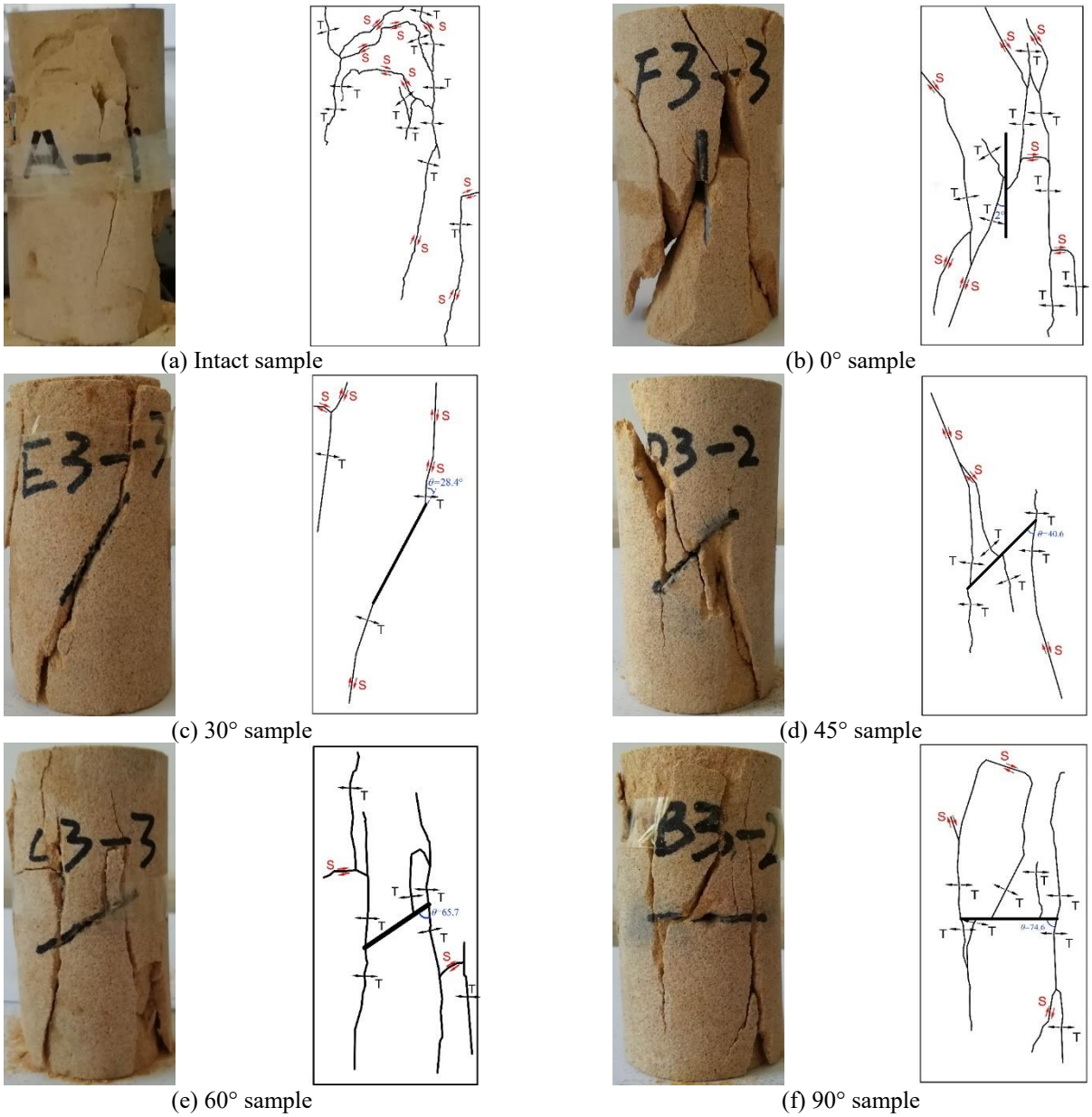

(a) Intact sample (b) 0° sample

(c) 30° sample (d) 45° sample

(e) 60° sample (f) 90° sample

Fig. 5 Failure modes of the cracked samples with different dip angles

initiation. The cracked samples with different dip angles all crack under tensile stress and wing cracks develop at the crack tips. The presence of a pre-fabricated crack alter the eventual mode of failure of the rock. As the dip angle increases, the sandstone's failure mode change from shear failure to tensile failure.

4. Discussion on the crack initiation mechanism

4.1 Mechanical analysis of crack initiation angle

The pre-fabricated crack surfaces in the rocks containing pre-fabricated cracks induce relative sliding under uniaxial compression. The concentrated tensile stress at the tip of the crack steadily increases, and micro-cracks initiate at the tip and gradually propagate along the crack propagation direction, forming a sliding-type tensile crack. As shown in Fig. 6, the stress state of the inclined crack surface under uniaxial compression (Liu 2019, Williams 1957) is

$$\begin{cases} \sigma_n = (1-C_n)\sigma \sin^2 \beta \\ \tau_n = (1-C_s)\sigma \sin \beta \cos \beta \end{cases} \tag{1}$$

where C_n and C_s are the crack pressure transmission and shear transmission coefficients, respectively , that is, $C_n = \dfrac{\pi a}{\pi a + \dfrac{E}{(1-\nu^2)k_n}}$, and $C_s = \dfrac{\pi a}{\pi a + \dfrac{E}{(1-\nu^2)k_s}}$.

Williams (1957) expressed the elastic stress field at the crack tip as

$$\sigma_{ij} = A_1 r^{-1/2} f_{ij}^1(\theta) + A_2 f_{ij}^2 + A_3 r^{1/2} f_{ij}^3(\theta) + \cdots \tag{2}$$

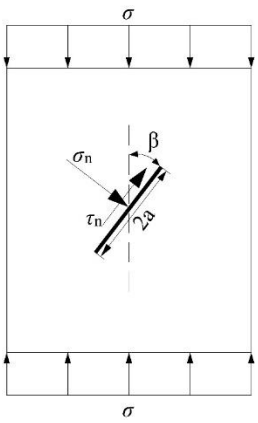

Fig. 6 Analysis of force in inclined cracks subjected to uniaxial compression

Where, the first term is a singular term and the second term is a non-singular term.

According to traditional fracture mechanics, only the influence of the first term on the stress field should be considered, while the second term can be neglected. However, under uniaxial compression, the crack initiation angle computed by using traditional maximum circumferential theory is always constant and is not related to the crack dip angle, which is manifestly impractical. Scholars have discovered (Zhao *et al*. 2018, Li *et al*. 2009, Huang *et al*. 2021) that *T*-stress has a significant effect on the propagation of cracks in rocks and that the *T*-stress should be included in the traditional fracture criteria. Therefore, according to the results of this study, the stress field at the closed crack tip (Fig. 7) should consist of both the stress intensity factor and three *T*-stress components, designated as T_x, T_y, and T_{xy}. This allows for the derivation of the expansion formula for the stress field at the tip of a type II crack in the polar coordinate system (Lu and Meshi 2014).

$$\begin{cases} \sigma_r = \dfrac{K_{II}}{2\sqrt{2\pi r}}(3\cos\theta - 1)\sin\dfrac{\theta}{2} + T_x\cos^2\theta + T_y\sin^2\theta + T_{xy}\sin(2\theta) \\ \sigma_\theta = -\dfrac{3K_{II}}{2\sqrt{2\pi r}}\sin\theta\cos\dfrac{\theta}{2} + T_x\sin^2\theta + T_y\cos^2\theta - T_{xy}\sin(2\theta) \\ \tau_{r\theta} = \dfrac{K_{II}}{2\sqrt{2\pi r}}\cos\dfrac{\theta}{2}(3\cos\theta - 1) + \dfrac{1}{2}\left(T_y - T_x\right)\sin 2\theta + T_{xy}\cos(2\theta) \end{cases} \quad (3)$$

where K_{II} is the stress intensity factor for type II cracks, and *r* is the material's critical crack area, which serves as a material performance parameter (Williams and Ewing 1972). The *T*-stress can be expressed as follows (Liu 2019) for the inclined crack shown in Fig. 6

$$\begin{cases} T_x = \sigma\cos^2\beta \\ T_y = \sigma\sin^2\beta \\ T_{xy} = \mu\sigma\sin^2\beta \end{cases} \quad (4)$$

where μ is the friction factor of the crack surface.

Under uniaxial compression, the two surfaces of a type II crack are in contact and are compressed, and the stress intensity factor can be

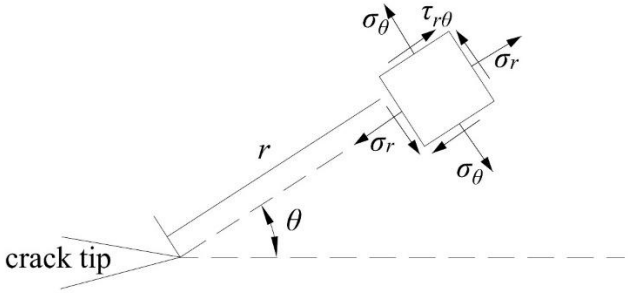

Fig. 7 Stress field at crack tip

$$K_{II} = \tau_{eff}\sqrt{\pi a} \quad (5)$$

where τ_{eff} is the effective shear stress. If the friction effect of the closed crack is considered, then

$$\tau_{eff} = \tau_n - \mu\sigma_n \quad (6)$$

According to the criteria for the maximum circumferential stress (Erdogan and Sih 1963), the crack propagates in the θ direction, which corresponds to the maximum value of σ_θ, and the value of θ obeys the following derivative relationship

$$\left.\frac{d\sigma_\theta}{d\theta}\right|_{r=r_0} = 0,\ \left.\frac{d^2\sigma_\theta}{d\theta^2}\right|_{r=r_0} < 0 \quad (7)$$

Based on Eqs. (2) and (6), Eq. (8) is obtained

$$-\frac{3K_{II}}{2\sqrt{2\pi r}}(\cos\theta\cos\frac{\theta}{2} - \frac{\sin\theta\sin\frac{\theta}{2}}{2}) + 2(T_x - T_y)\sin\theta\cos\theta - 2T_{xy}\cos(2\theta) = 0 \quad (8)$$

The sample is subjected to uniaxial compression, where $2a$= 3.0 cm, and r= 0.554 mm. Through mechanical tests conducted on the cracked sandstone samples with different dip angles, the average values of the test parameters *E*, ν and μ were found to be $\overline{E}$ = 6.628 GPa, $\bar{\nu}$ = 0.28, and μ= 0.432. The values of the other parameters were chosen based on experience: k_n = 2 GPa/cm, and k_s = 1 GPa/cm. The relationship between the crack dip angle β and the crack initiation angle θ can be obtained by substituting Eqs. (1), (4), (5), and (6) into Eq. (8) (Fig. 8).

According to the findings of the fracture mechanics calculations, both the theoretical and experimental values of the crack initiation angle increase as the crack dip angle increases. Only the 30° and 45° samples had large errors (13.24° and 18.73°, respectively) due to the impact of the shear stress at the ends of the sample; whereas the errors of the other samples are all less than 5°. When the dip angle of the pre-fabricated crack is β = 0°, the crack initiation angle is $\theta \approx$ 2° (Fig. 5(b)), and the initiated crack propagate in the external load direction without forming a thorough crack. For moderate dip angles of β = 30° and β = 45°, the shear stress produce at the top and lower ends of the sample during the compression process has a significant impact on the crack initiation, resulting in the experimental value being smaller than the theoretical value. When the dip angle

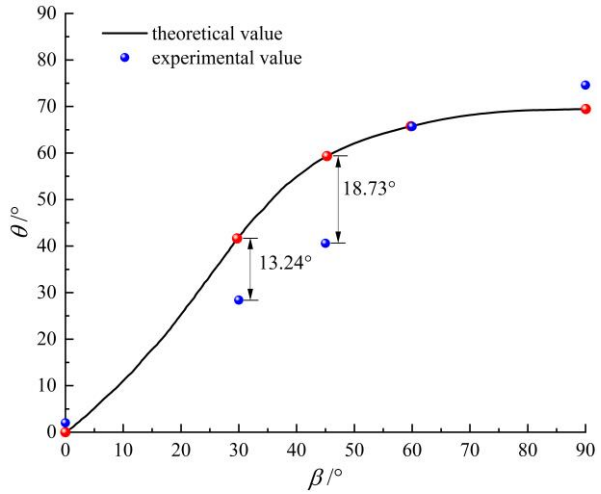

Fig. 8 Relationship between crack initiation angle θ and crack dip angle β

is $\beta = 90°$ and the initiation angle is $\theta \approx 74.6°$ (Fig. 5(f)), the initiated crack propagates along the loading direction and cause failure of the sample.

4.2 Fracture strength of cracked rocks

As the axial pressure σ progressively increases and reaches a certain strength under uniaxial compression, the pre-fabricated crack tip starts to initiate in a certain direction. In order to study the influence of the crack dip angle on the crack initiation strength, the rock's fracture strength is defined as

$$k_{cr} = \sigma_{ci}\sqrt{\pi a} \tag{9}$$

where σ_{ci} is the crack initiation stress.

By substituting Eqs. (1) and (6) into Eq. (7), it is obtained

$$K_{II} = \frac{\sigma}{2}[(1-C_s)\sin 2\beta - 2\mu(1-C_n)\sin^2\beta]\sqrt{\pi a} \tag{10}$$

According to fracture mechanics, the critical condition for crack initiation is $|K_{II}| = K_{IIc}$, and the initiation stress can be obtained using Eq. (11)

$$\sigma_{ci} = \frac{2K_{IIc}}{[(1-C_s)\sin 2\beta - \mu(1-C_n)(1-\cos 2\beta)]\sqrt{\pi a}} \tag{11}$$

According to Eqs. (8) and (10), the fracture strength k_{cr} varies with the dip angle β of the crack, demonstrating a nonlinear change law, and minima of k_{crmin} exist. According to the minima's compliance with the conditions is

$$\frac{\partial k_{cr}}{\partial \beta} = 0,\ \frac{\partial^2 k_{cr}}{\partial \beta^2} > 0 \tag{12}$$

By substituting Eqs. (9) and (11) into Eq. (12), the dip angle of the crack corresponding to k_{crmin} can be obtained as

$$\begin{cases} \beta_m = \dfrac{1}{2}\arctan\dfrac{A}{\mu B} \\ A = 1 - C_s \\ B = 1 - C_n \end{cases} \tag{13}$$

Eq. (13) demonstrates that under uniaxial compression, when the crack dip angle β is β_m, the stress intensity factor K_{II} is the maximum value, the crack tip is most susceptible to crack initiation, and the crack initiates and grows near the tip. Thus, β_m can be defined as the superior crack angle.

According to trigonometric functions, Eq. (14) can be obtained through transformation

$$\sin 2\beta = \frac{1}{\sqrt{1+\left(\dfrac{\mu A}{B}\right)^2}},\ \cos 2\beta = \frac{\dfrac{\mu A}{B}}{\sqrt{1+\left(\dfrac{\mu A}{B}\right)^2}} \tag{14}$$

Combining Eqs. (9), (11), and (14), it is obtained

$$k_{crmin} = \frac{2K_{IIc}\sqrt{1+\left(\dfrac{\mu A}{B}\right)^2}}{A - \mu B\left(\sqrt{1+\left(\dfrac{\mu A}{B}\right)^2} - \dfrac{\mu A}{B}\right)} \tag{15}$$

By using k_{crmin} to normalize k_{cr}, the results can be obtained

$$\frac{k_{cr}}{k_{cr\,\min}} = \frac{A - \mu B\left(\sqrt{1+\left(\dfrac{\mu A}{B}\right)^2} - \dfrac{\mu A}{B}\right)}{[A\sin 2\beta - \mu B(1-\cos 2\beta)](1+\sqrt{1+\left(\dfrac{\mu A}{B}\right)^2})} \tag{16}$$

Eq. (16) demonstrates that the normalized value of k_{cr} varies with the value of β, and the features of this variation are related to the crack surface friction factor μ, as well as the pressure transmission C_n and shear transmission C_s coefficients.

The parameters of the cracked sandstone samples obtained through mechanical tests are μ = 0.41–0.48, C_n=0.75–0.77, and C_s=0.62-0.64. Representative values of these parameters were taken as follows: ①μ=0.41, C_n=0.75, and C_s=0.62; ②μ =0.41, C_n=0.77, and C_s=0.64; ③μ =0.45, C_n=0.75, and C_s=0.62; ④μ =0.45, C_n=0.77, and C_s=0.64; ⑤μ=0.48, C_n=0.75, and C_s=0.62; and ⑥μ =0.48, C_n=0.77, and C_s=0.64. These sets of values were substituted into Eq. (16) to plot the curve of the $k_{cr}/k_{crmin} - \beta$ relationship (Fig. 9).

Fig. 9 shows that the value of β_m corresponding to k_{crmin} varies between 36.2 and 36.6, which is similar to the crack dip angle of 30° for the lowest crack initiation stress level measured above, thus validating the accuracy of the AE signal in describing crack initiation. As β gradually increases, the whole curve exhibits a U-shaped change trend. For various β intervals, the change trend of k_{cr}/k_{crmin} with β varies somewhat. When β < 36.2, the curves

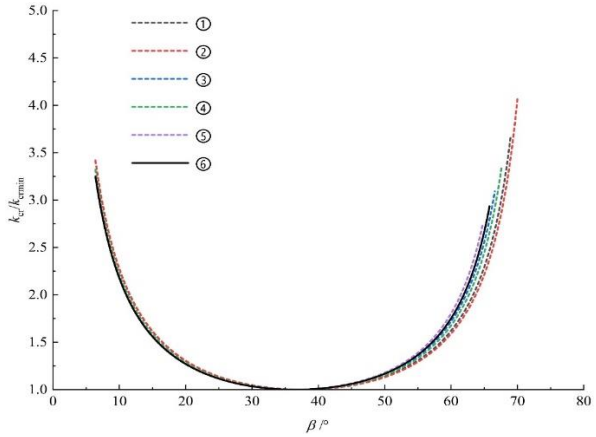

Fig. 9 Variation of k_{cr}/k_{crmin} with the crack dip angle

are generally close. When β > 36.6, the distance between the curves increases, and β has a significant influence on k_{cr}/k_{crmin} in this interval, indicating that the fracture intensity of the rock is affected by the loading direction and crack surface angle. By comparing two sets of representative values, i.e., ①, ③, and ⑤ and ②, ④, and ⑥, it is found that while C_n and C_s remain constant, β_m decreases with increasing μ, indicating that the superior crack angle when fracturing is most probably related to the properties of the crack surface. By comparing three sets of representative values, i.e., ① and ②, ③ and ④, and ⑤ and ⑥, it was found that when μ is held constant, β_m increases with increasing C_n and C_s, suggesting that the superior fracture angle is related to the rock's properties.

5. Discussion on the meso-crack evolution characteristic

Based on the analysis of the crack initiation characteristics, the differences in the mechanical characteristics caused by the rock's crack dip angle during the crack initiation process are found to be significant. Moreover, it is impossible to fully observe the meso-crack activity and changes throughout the entire failure process using only theoretical analysis. Consequently, in this study, the AE data were used to analyze the crack propagation characteristics of the pre-fabricated cracked sandstone samples in detail.

5.1 Meso-crack characteristic theory

5.1.1 AE energy: Crack strength characteristic

The AE energy is the excess energy released when the defect movement or movement is blocked. The number of AE energy events detected can represent the strength characteristics of meso-crack fracture (Wang *et al*. 2019).

As can be seen from Fig. 10, the AE energy is represented by the area bounded by the signal envelope and the coordinate axis.

For a cracking event, the AE energy count rate is calculated as

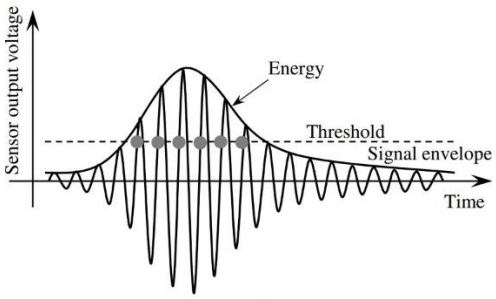

Fig. 10 Acoustic emission signal waveform

$$E = \frac{1}{Rt}\int_0^{\infty} U(t)^2 dt \tag{17}$$

where R is the input impedance of the voltage measurement line, and $U(t)$ is the voltage, which varies with time.

5.1.2 b-value: crack scale characteristic

When Gutenburg and Richter investigated the law of seismic activity in 1944, they discovered a link between the change in the *b*-value and the crack size, and they developed the Gutenburg-Richter (G-R) relationship based on the magnitude-frequency relationship (Gutenberg and Richter 1944)

$$\lg N = a - bM \tag{18}$$

where M is the magnitude of the earthquake intensity, N is the number of earthquakes with a magnitude greater than M, and a and b are constants. Rock fractures and seismic plates have significant differences in geometric scale, time scale, and boundary conditions, but their AE phenomena and seismic waves are similar (Garcimartin *et al*. 1997). In research on AE of rock materials, the above formula has also been frequently used, but the amplitude of the AE is typically divided by 20 to replace the magnitude M

$$M_L = A/20 \tag{19}$$

where M_L is the magnitude of the AE, and A is the AE amplitude.

5.1.3 RA-AF: crack classification characteristic

Ohtsu *et al*. (2007) discovered that there is a strong correlation between the rock crack type and the RA–AF , where RA is the ratio of the rise time to the peak amplitude, and the average frequency (AF) is the ratio of the ringing count to the duration. In the Japanese JCMS-III B5706 concrete building code (RILEM Technical Committee (RILEM Technical Committee (Masayasu Ohtsu)** 2010) the slope of the dividing line (AF/RA) in Fig. 11 is defined as k, the shear rupture signal is defined as AF/RA < *k*, and the tension rupture signal is defined as AF/RA > *k*.

5.2 Evolution of meso-cracks in cracked sandstone

5.2.1 Evolution of meso-crack strength

Fig. 12 depicts the evolution of the micro-crack strength of the intact sandstone and cracked sandstone samples

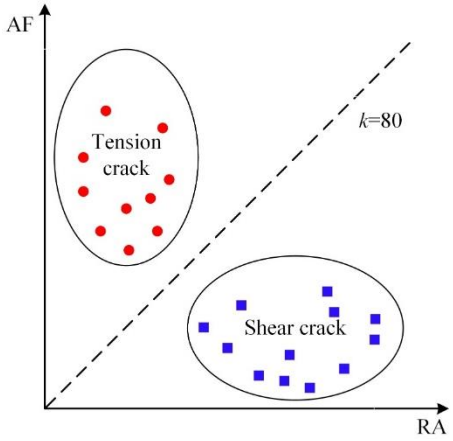

Fig. 11 Determination of the crack type based on *RA-AF*

(taking the 0° sample as an example). The analysis reveals that the changes in the AE energy count rate of the intact sample and the cracked sample can be divided into three stages: the AE quiet period, the steady growth period, and the low growth period. In the initial loading period, the closure and sliding of the original micro-cracks release a small amount of elastic stress waves, and the amount of AE energy released at this point is extremely small. Before point a (the AE quiet period), the AE signal is extremely weak, and there are essentially no rock fractures. When the stress exceeds the crack initiation stress σ_{ci}, it enters the stable growth period of AE, and the micro-cracks in the cracked sample initiate in the vicinity of the pre-fabricated crack tip, but the crack propagation speed is extremely slow, and the AE energy count rate increases at a slow rate. When the stress exceeds point b, it enters the AE low or high growth period, the accumulated energy meets the critical value for accelerated crack growth, and the local crack expands at an accelerated rate. At this point, the cumulative AE energy growth rate of the cracked sample is greater than that of the intact sample. According to the crack initiation characteristics analysis of cracked rock sample in section 3, because the stress is initially concentrated at the crack tip, the accumulated strain energy can be released rapidly, and the crack rupture strength is high. In contrast, the accumulated strain energy of the intact sample is distributed throughout the entire sample, and the crack rupture is not a concentrated breakout. Thus, the crack's rupture strength is relatively low. The AE energy characterizes the rupture strength of the meso-cracks; so, the staged characteristics of the evolution of the mesoscopic crack strength of the intact sample and the cracked sample can be divided into low strength, medium strength, and medium-high strength; and low strength, medium strength, and high strength, respectively. The experiments reveal that the initial initiation and expansion of the micro-cracks only occurred at the end of the AE steady growth period (point b). Consequently, AE energy is superior to macro-strength characteristics and direct observation methods in detecting the evolution characteristics of meso-cracks in rocks.

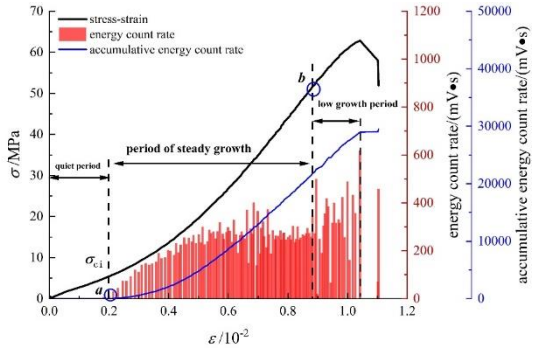

(a) Intact sample

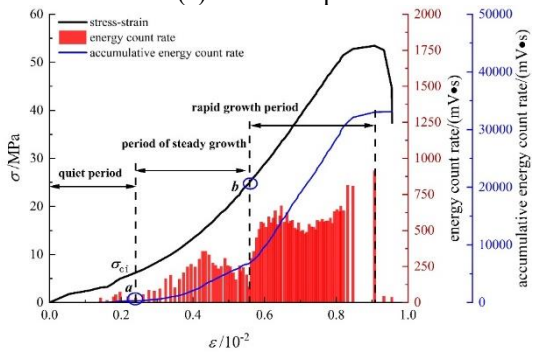

(b) 0° sample

Fig. 12 Meso-crack strength characteristics of the sandstone samples

5.2.2 Evolution characteristics of meso-crack scale

In accordance with the frequency of the AE signal measured in the experiment, 1000 AE events were sampled to estimate the *b*-value in order to prevent deterioration of the reliability of the calculated *b*-value due to the use of a sampling window that is too narrow. Eqs. (18) and (19) are used to calculate the *b*-value of the AE in this study. The last instant of each sample window is used as the scale of the *b*-value throughout data processing. Fig. 13 shows the characteristics of the evolution of meso-cracks in the intact and cracked samples. According to the degree of fluctuation of the *b*-value, the *b*-value of the intact sample was divided into two stages: the increasing-fluctuating period and the abrupt-decreasing period (divided by the blue dotted line in Fig. 13). During the increasing-fluctuation period, the *b*-value increase overall. Even when the *b*-value decrease due to a small number of large-scale cracks, the small-scale cracks continue to predominate and the small-scale meso-cracks are fully developed. With the accumulation and penetration of the small-scale cracks during the abrupt-decreasing period, large-scale cracks developed, and a massive amount of energy is released, resulting in the sudden instability of the rock. At this point, the *b*-value decreased abruptly.

In contrast to the intact sample, the cracked sample's *b*-value evolution is divided into three distinct stages: the increasing period, the decreasing-fluctuating period, and the abrupt-decreasing period. In the initial stage of loading, the *b*-value increase, the pre-existing cracks are compressed and closed, and small-scale cracks predominate. When the stress exceeds the crack initiation stress σ_{ci}, micro-cracks

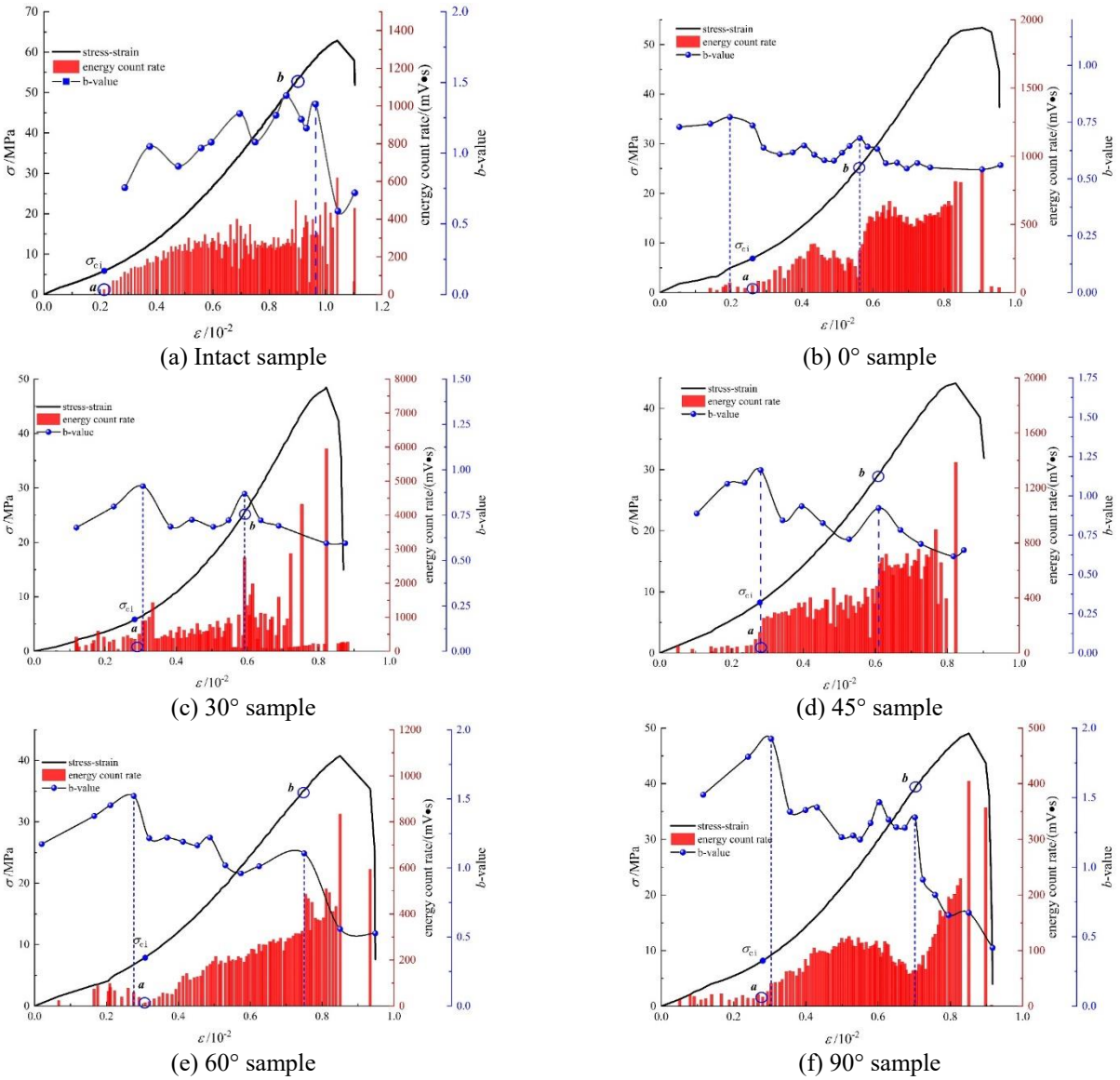

(a) Intact sample (b) 0° sample

(c) 30° sample (d) 45° sample

(e) 60° sample (f) 90° sample

Fig. 13 Meso-crack scale characteristics of the sandstone samples

accumulated preferentially in the stress concentration zone at the crack tip, the cracks germinate and initiate to produce local large-scale cracks, and the *b*-value decreased for the first time. Subsequently, the sandstone's meso-cracks continued to spread at a very slow pace. Even while the small-scale cracks continue to develop, the large-scale cracks still predominate, and the *b*-value fluctuate with an overall downward trend. When the loading stress approach point b, surface cracks in the sandstone that are visible to the naked eye germinate and propagate. At this point, the *b*-value decrease for the second time and enter the abrupt decrease period. There is a strong relationship between the scale characteristics and the strength characteristics of meso-cracks, and both can represent the propagation and evolution characteristics of meso-cracks from different angles.

5.2.3 Evolution of meso-crack type

In order to more intuitively reflect the changes in the crack rupture type throughout the entire loading process, in this study, k= 80 was selected as the slope of the boundary line of the tension-shear rupture signal, and the sampling window was set as 100 AE events (Aggelis 2011, Wang *et al*. 2021). By dividing the number of shear cracks by the number of tension cracks in every 100 AE events, r= RA/AF was used in the analysis of meso-crack type evolution (Gan *et al*. 2020). The ratio of shear cracks increase as r increase. When r > 1, shear cracks predominate; and vice versa.

Fig. 14 shows the evolution characteristics of the types of meso-cracks in the intact sandstone and cracked sandstone samples. The figure shows that the *r*-value of the intact samples and the cracked samples show distinct evolution laws. The top and bottom ends of the sample are influenced by the shear force, the shear cracks expand rapidly when the crack initiation stress σ_{ci} is attained, and the *r*-value increase. When the stress exceed point b, the shear cracks grow quickly, the *r*-value increase

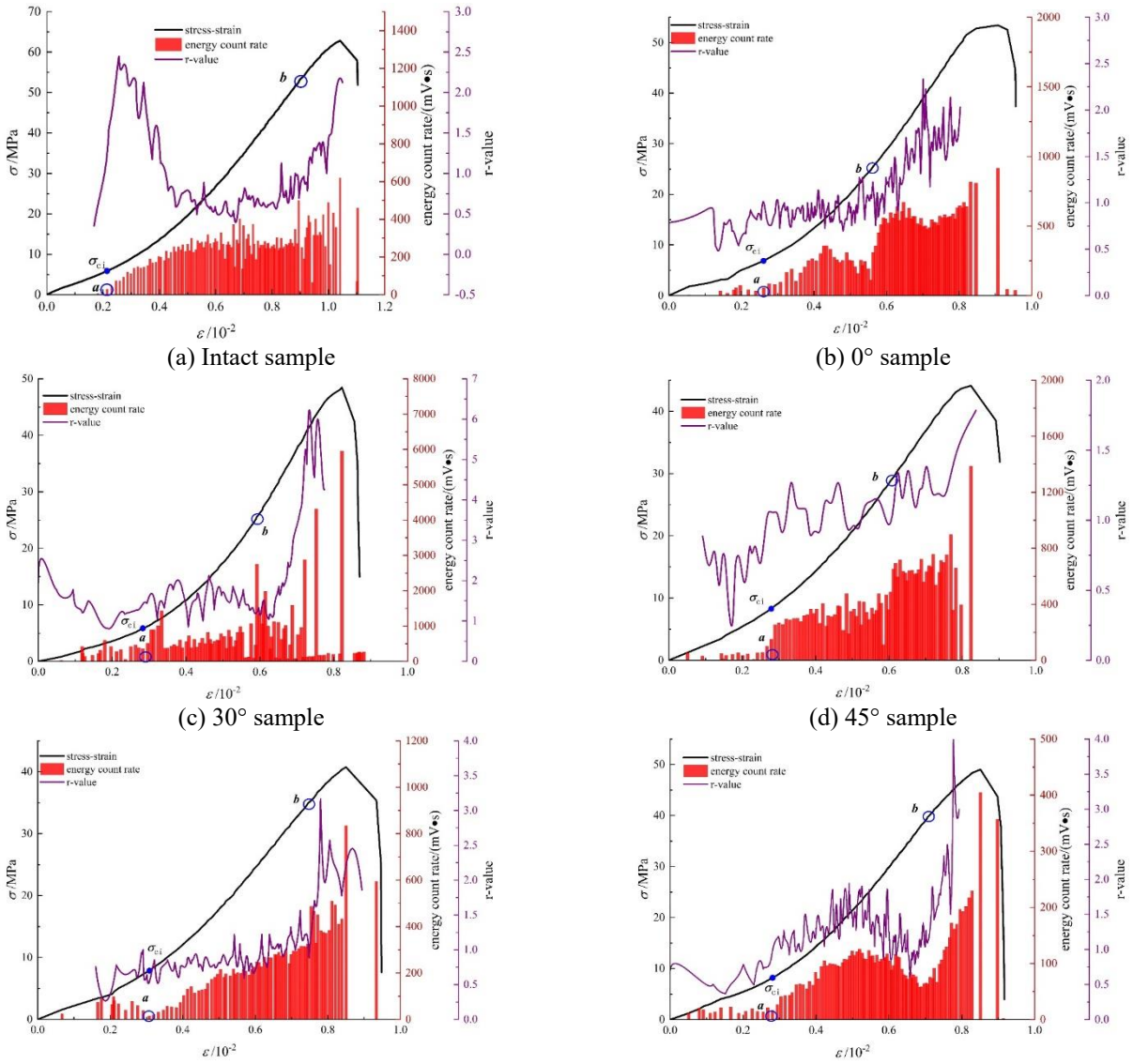

(a) Intact sample (b) 0° sample

(c) 30° sample (d) 45° sample

(e) 60° sample (f) 90° sample

Fig. 14 Meso-crack type characteristics of the sandstone samples

substantially, and the rock become unstable and fails. Due to the presence of pre-fabricated cracks, the cracked samples initially experience stress concentration at the crack tip, and the tensile crack initiates at the crack tip. Near the crack initiation stress σ_{ci}, the *r*-values of the cracked samples remain low or decreased, indicating that the tension cracks increase or predominate when crack initiation occurs at the crack tip. When the dip angle of the crack is <45°, it is readily influenced by the shear stress at the top and bottom ends of the sample, and the *r*-value is significantly greater. When the stress exceeds point b, the *r*-value quickly increases, and the shear crack grows until the rock failed.

From this perspective, the study of the evolution characteristics of the meso-crack types and the analysis of the macroscopic failure mode of sandstone in Section 3.2 yields comparable findings. The tension crack initiates the formation of the wing crack at the crack tip, followed by the growth and expansion of the shear crack to produce the macroscopic main crack and several failure modes. In addition, the *r*-value has a good correlation with the AE energy. The increase in the *r*-value is accompanied by an increase in the shear cracks and the release of a large amount of energy, indicating that the meso-crack type is highly correlated with the meso-crack strength.

6. Conclusions

The presence, propagation, and coalescence of cracks in engineering rock masses can result in rock failure, even posing a threat to the stability of underground engineering structures. Therefore, investigating the initiation mechanism and evolution law of cracks in cracked rocks is of great significance. In this study, theoretical and experimental studies were conducted on sandstone specimens with cracks of different dip angles. Based on fracture mechanics, the influence of crack dip angle on the initiation mechanism

was studied. The evolution law of meso-cracks was investigated using the theory of micro-crack characteristics. The main conclusions of this study are as follows:

- Based on fracture mechanics, the maximum circumferential stress criteria considering *T*-stress were established. The connection between the crack initiation angle θ and crack angle β increases as the calculated crack angle β increases, and the theoretical values are in excellent agreement with the experimental values. Based on fracture mechanics, the functional relationship between rock fracture strength and crack dip angle was derived. The fracture strength k_{cr} of sandstone exhibits a U-shaped trend as the fracture angle β increases. The fracture angle that is most susceptible to crack initiation is defined as the superior crack angle β_m, which is between 36.2 and 36.6 and is dependent on the properties of the rock and the rock fracture plane.
- The AE energy can identify the evolution characteristics of meso-cracks in rocks better than the macroscopic strength characteristics and direct observation methods. The characteristics of the meso-crack strength evolution stages of the intact and cracked rocks can be divided into low strength, medium strength, and medium-high strength; and low strength, medium strength, and high strength, respectively.
- The *b*-value evolution of the intact rock and the cracked rock is divided into two periods and three periods, respectively. For the intact rock, the small-scale cracks fully develop until macro-cracks form on the rock surface, and the high strength and large-scale cracks expand rapidly. In the cracked rock, the cracks initiate at the crack tip first, where large-scale cracks congregate, and the *b*-value decreases for the first time. Then, when macro-cracks emerge on the surface of the rock, the large-scale cracks grow rapidly, the *b*-value decrease again, and the rock becomes unstable.
- Near the crack initiation stress σ_{ci}, the *r*-value of the intact rock increases rapidly, and the shear cracks increase and then decrease. When the stress exceeds point b, the *r*-value increases significantly and the shear cracks increase quickly. The *r*-values of the cracked rocks remain low or decreased near σ_{ci}, and the tensile cracks increase or dominate when cracks initiated at the crack tip. When the stress exceeds point b, the *r*-value quickly increases, and the high strength shear crack increases substantially until the rock fails. The AE parameters can be used to evaluate the internal crack evolution in a sandstone in terms of the meso-crack intensity scale and type.

Acknowledgments

This work was supported by the Natural Science Foundation of Hunan Province, China(Grant No.2021JJ30575), and National Natural Science Foundation of China(Grant No. 51204098).

References

Aggelis, D.G. (2011), "Classification of cracking mode in concrete by acoustic emission parameters", *Mech. Res. Commun*., **38**(3), 153-157. https://doi.org/10.1016/j.mechrescom.2011.03.007.

Aliha, M.R.M., Mahdavi, E. and Ayatollahi, M.R. (2017), "The influence of specimen type on tensile fracture toughness of rock materials", *Pure. Appl. Geophys.,* **174**(3), 1237-1253. https://doi.org/10.1007/s00024-016-1458-x.

Abdollahipour, A., Marji, M.F., Bafghi, A.Y. and Gholamnejad, J. (2016), "Time-dependent crack propagation in a poroelastic medium using a fully coupled hydromechanical displacement discontinuity method", *Int. J. Fract.,* **199**, 71-87. https://doi.org/10.1007/s10704-016-0095-9.

Abdollahipour, A. and Marji, M.F. (2020), "A thermo-hydromechanical displacement discontinuity method to model fractures in high-pressure, high-temperature environments", *Renew. Energ..,* **153**, 1488-1503. https://doi.org/10.1016/j.renene.2020.02.110.

Eberhardt, E., Stead, D., Stimpson, B. and Read, R.S. (1998), "Identifying crack initiation and propagation thresholds in brittle rock", *Can. Geotech. J*., **35**(2), 222-233. https://doi.org/10.1139/t97-09.

Erdogan, F. and Sih, G.C. (1963), "On the crack extension in plates under plane loading and transverse shear", *J. Basic. Eng.,* https://doi.org/10.1115/1.3656897.

Gan, Y.X., Wu, S.C., Ren, Y. and Zhang, G. (2020), "Evaluation indexes of granite splitting failure based on RA and AF of AE parameters", *Rock. Soil. Mech*., **41**(7), 2324-2332. http://dx.doi.org/10.16285/j.rsm.2019.1460.

Ganne, P., Vervoort, A. and Wevers, M. (2007), "Quantification of pre-peak brittle damage: Correlation between acoustic emission and observed micro-fracturing", *Int. J. Rock. Mech. Min. Sci.,* **44**(5), 720-729. https://doi.org/10.1016/j.ijrmms.2006.11.003.

Garcimartin, A., Guarino, A., Bellon, L. and Ciliberto, S. (1997), "Statistical properties of fracture precursors", *Phys. Rev. Lett*., **79**(17), 3202. https://doi.org/10.1103/PhysRevLett.79.3202.

Guo, Q.F., Wu, X., Cai, MF., Ren, F.H. and Pan, J.L. (2019), "Crack initiation mechanism of pre-existing cracked granite", *J. China. Coal. Soc.,* **44**(S2), 476-483. http://dx.doi.org/10.13225/j.cnki.jccs.2019.1212.

Gutenberg, B. and Richter, C.F. (1944), "Frequency of earthquakes in California", *Bull. Seismol. Soc. Am.*, **34**(4), 185-188. https://doi.org/10.1785/BSSA0340040185.

Haeri, H., Sarfarazi, V., Ebneabbasi, P., Shahbazian, A., Marji, M.F. and Mohamadi, A.R. (2020), "XFEM and experimental simulation of failure mechanism of non-persistent joints in mortar under compression", *Constr. Build. Mater.*, **236**, 117500. https://doi.org/10.1016/j.conbuildmat.2019.117500.

Huang, S.Y., Wang, J.J., Wang, A.G., Ji, E.Y., Guo, W.L. and Ji, S.Y. (2021), "Fracture failure mechanism and fracture criterion of compacted clay under compression and shear action", *Chin. J. Geotech. Eng*., **43**(3), 492-501. http://dx.doi.org/10.11779/CJGE202103012.

Kim, J.S., Lee, K.S., Cho, W.J., Choi, H.J. and Cho, G.C. (2015), "A comparative evaluation of stress–strain and acoustic emission methods for quantitative damage assessments of brittle rock", *Rock. Mech.*, **48**(2), 495-508. https://doi.org/10.1007/s00603-014-0590-0.

Li, X., Liang, Y., Luo, Y. and Ai, C. (2020), "Predicting hydraulic fracture propagation based on maximum energy release rate theory with consideration of T-stress", *Fuel*., **269**, 117337. https://doi.org/10.1016/j.fuel.2020.117337.

Li, N., Sun, W., Huang, B., Chen, D., Zhang, S. and Yan, M. (2021), "Acoustic emission source location monitoring of laboratory-scale hydraulic fracturing of coal under true triaxial stress", *Nat. Resour. Res.,* **30**, 2297-2315.

https://doi.org/10.1007/s11053-021-09821-9.

Li, X.F., Liu, G.L. and Lee, K.Y. (2009), "Effects of T-stresses on fracture initiation for a closed crack in compression with frictional crack faces", *Int. J. Fract.,* **160**(1), 19-30. https://doi.org/10.1007/s10704-009-9397-5.

Lin, B.S. (1985), "The mixed mode brittle fracture criteria in siliding mode fracture", *Appl. Math. Mech.,* **6**(11), 1061-1067. https://doi.org/10.1007/BF03250505.

Liu, H.Y. (2019), "Initiation mechanism of cracks of rock in compression and shear considering T-stress", *Chin. J. Geotech. Eng.,* **41**(07), 1296-1302. http://dx.doi.org/10.11779/CJGE201907014.

Liu, X.L., Liu, Z., Li, X.B. and Han, M.S. (2019), "Acoustic emission b-values of limestone under uniaxial compression and Brazilian splitting loads", *Rock. Soil. Mech*., **40**(1), 267-274. http://dx.doi.org/10.16285/j.rsm.2018.2161.

Lu, K. and Meshii, T. (2014), "Three-dimensional T-stresses for three-point-bend specimens with large thickness variation", *Eng, Fract, Mech.,* **116**(1), 197-203. https://doi.org/10.1016/j.engfracmech.2013.12.011.

Martin, C.D. and Chandler, N.A. (1994), "The progressive fracture of Lac du Bonnet granite", *Int. J. Rock. Mech. Min. Sci.,* **31**(6), 643-659. https://doi.org/10.1016/0148-9062(94)90005-1.

Ohtsu, M., Isoda, T. and Tomoda, Y. (2007), "Acoustic emission techniques standardized for concrete structures", *Phys. Rev. lett.,* **25**, 21-32. https://doi.org/10.4028/www.scientific.net/AMR.13-14.183.

Rezanezhad, M., Lajevardi, S.A. and Karimpouli, S. (2020), "Effects of pore (s)-crack locations and arrangements on crack growth modeling in porous media", *Theor. Appl. Fract. Mech.*, **107**, 102529. https://doi.org/10.1016/j.tafmec.2020.102529.

Rezanezhad, M., Lajevardi, S.A. and Karimpouli, S. (2021), "Application of equivalent circle and ellipse for pore shape modeling in crack growth problem: A numerical investigation in microscale", *Eng. Fract. Mech.,* **253**, 107882. https://doi.org/10.1016/j.engfracmech.2021.107882.

RILEM Technical Committee (Masayasu Ohtsu)**. (2010), "Recommendation of RILEM TC 212-ACD: acoustic emission and related NDE techniques for crack detection and damage evaluation in concrete*", *Mater. Struct.*, **43**(9), 1183-1186. https://doi.org/10.1617/s11527-010-9638-0.

Sun, B., Yang, P., Liu, S. and Zeng, S. (2023), "Impact dynamic characteristics and constitutive model of granite damaged by cyclic loading", *J. Mater. Res. Technol.*, **24**, 333-345. https://doi.org/10.1016/j.jmrt.2023.03.047.

Shlyannikov, V.N. (2013), "T-stress for crack paths in test specimens subject to mixed mode loading", *Eng. Fract. Mech.,* **108**, 3-18. https://doi.org/10.1016/j.engfracmech.2013.03.011.

Sun, B., Yang, H., Fan, J., Liu, X. and Zeng, S. (2023), "Energy evolution and damage characteristics of rock materials under different cyclic loading and unloading paths", *Buildings.,* **13**(1), 238. https://doi.org/10.3390/buildings13010238.

Sih, G.C. (1974), "Strain-energy-density factor applied to mixed mode crack problems", *Int. J. Fract*., **10**(3), 305-321. https://doi.org/10.1007/BF00035493.

Sun, B., Liu, S., Zeng, S., Wang, S.Y. and Wang, S.P. (2021), "Dynamic characteristics and fractal representations of crack propagation of rock with different fissures under multiple impact loadings", *Sci. Rep.*, **11**(1), 1-16. https://doi.org/10.1038/s41598-021-92277-x.

Tang, S.B. (2015), "The effect of T-stress on the fracture of brittle rock under compression", *Int. J. Rock. Mech. Min. Sci.,* **79**, 86-98. https://doi.org/10.1016/j.ijrmms.2015.06.009.

Wang, C.L., Hou, X.L., Li, H.T., Zhang, S.J. and Tao, G. (2019), "Experimental investigation on dynamic evolution characteristics of micro-cracks for sandstone rocks under uniaxial compression", *Chin. J. Geotech. Eng.,* **41**(11), 2120-2125. http://dx.doi.org/10.11779/CJGE201911018.

Wang, G.L., Wang, R.Q., Sun, F. and Cao T.C. (2021), "Study on RA-AF characteristics of acoustic emission and failure mode of karst-fissure limestone under uniaxial compression", *China. J. Highw. Transp.*, **35**(08), 1-13. http://kns.cnki.net/kcms/detail/61.1313.U.20211025.1428.002.html.

Wang, J., Li, Y., Song, W.D. and Xu, W.B. (2019), "Analysis of damage evolution characteristics of jointed rock mass with different joint dip angles", *J. Harbin. Inst. Technol.,* **51**(8), 143-150. http://dx.doi.org/10.11918/j.issn.0367-6234.201805091.

Wang, M., Shao, X., Zhu, L. and Zhou, Z. (2021), "Use of acoustic emission to determine the effects of bedding and stress paths on micro-cracking evolution of anisotropic shale under cyclic loading tests", *Environ. Earth. Sci.,* **80**(15), 1-14. https://doi.org/10.1007/s12665-021-09761-w.

Wei, M., Dai, F., Liu, Y., Li, A. and Yan, Z. (2021), "Influences of loading method and notch type on rock fracture toughness measurements: from the perspectives of T-stress and fracture process zone", *Rock. Mech*., **54**(9), 4965-4986. https://doi.org/10.1007/s00603-021-02541-9.

Williams, M.L. (1957), "On the stress distribution at the base of a stationary crack", *J. Appl. Mech.,* **24**(1), 109-114. https://doi.org/10.1115/1.4011454.

Williams, J.G. and Ewing, P.D. (1972), "Fracture under complex stress-the angled crack problem", *Int. J. Fract. Mech.,* 8(4), 441-446. https://doi.org/10.1007/BF00191106.

Wu, H., Dai, B., Cheng, L., Lu, R., Zhao, G. and Liang, W. (2021), "Experimental study of dynamic mechanical response and energy dissipation of rock having a circular opening under impact loading", *Min. Metall. Explor.,* **38**(2), 1111-1124. https://doi.org/10.1007/s42461-021-00405-y.

Wu, H., Ma, D., Spearing, A.J.S. and Zhao, G. (2021), "Fracture response and mechanisms of brittle rock with different numbers of openings under uniaxial loading", *Geomech. Geoeng*., **25**(6), 481-493. https://doi.org/10.12989/gae.2021.25.6.481.

Yuan, Y., Fu, J.L., Wang, X.L. and Shang, X. (2020), "Experimental study on mechanical properties of prefabricated single-cracked red sandstone under uniaxial compression", *Adv. Civ. Eng.*, **2020**. https://doi.org/10.1155/2020/8845368.

Zhang, G., Wang, M., Li, X., Yue, S., Wen, Z. and Han, S. (2021), "Micro- and macrocracking behaviors in granite and molded gypsum containing a single flaw", *Constr. Build. Mater.,* **292**, 123452. https://doi.org/10.1016/j.conbuildmat.2021.123452.

Zhang, Y.B., Zhang, X., Liang, P., Sun, L., Yao, X.L., Liu, X.X. and Liang, J.L. (2019), "Experimental research on time-frequency characteristics of AE P-wave and S-wave of granite under failure process", *Chin. J. Rock. Mech. Eng.,* **38**(2), 3554-3564. https://doi.org/10.13722/j.cnki.jrme.2019.0250.

Zhao, Y.L., Fan, Y., Zhu, Z.M., Zhou, C.L. and Qiu, H. (2018), "Analytical and experimental study on the effect of T-stress on behavior of closed cracks", *Chin. J. Rock. Mech. Eng.,* **37**(6), 1340-1349. https://doi.org/10.13722/j.cnki.jrme.2017.1563.

CC